MDPI

Article

AlSi10Mg/AlN Interface Grain Structure after Laser Powder Bed Fusion

Ivan A. Pelevin [1,*], **Dmitriy Yu. Ozherelkov** [1], **Anton Yu. Nalivaiko** [1,2], **Anna I. Bodyakova** [3], **Stanislav V. Chernyshikhin** [1,4], **Boris O. Zotov** [1], **Andrey V. Korshunov** [1,5] and **Alexander A. Gromov** [1]

1   Catalysis Lab., National University of Science and Technology MISIS, Leninsky Avenue 4, Moscow 119049, Russia
2   University Administration, Moscow Polytechnic University, Bolshaya Semyonovskaya 38, Moscow 107023, Russia
3   Laboratory of Mechanical Properties of Nanoscale Materials and Superalloys, Belgorod State University, 85 Pobedy Street, Belgorod 308015, Russia
4   Center for Design, Manufacturing and Materials, Skolkovo Institute of Science and Technology, Moscow 121205, Russia
5   Department of Building Materials, Moscow State University of Civil Engineering, 26, Yaroslavskoye Shosse, Moscow 129337, Russia
*   Correspondence: i.pelevin@misis.ru

Abstract: Details and features of the grain structure near the interface region between the AlN ceramic phase and AlSi10Mg matrix after the laser powder bed fusion (LPBF) were investigated. Aluminum nitride particles were obtained through self-propagating high-temperature synthesis and mechanically mixed with aluminum matrix powder. Optimization of the LPBF process parameters resulted in synthesized material free of pores and other defects. Optical microscopy analysis of etched cross-section and more detailed EBSD analysis revealed regions with relatively coarse grains at melting pool boundaries and fine grains in the melt pool core and near the AlN particles. More-over, a pronounced orientation of fine elongated matrix grains towards the center of the ceramic particle was obtained. The such formed microstructure is attributed to directional heat sink during crystallization due to the higher thermal conductivity of aluminum nitride compared to the AlSi10Mg matrix. On the contrary, poor wettability of AlN by melt partly prevented the formation of such features, thus a combination of these factors determines the final microstructure of the interface in the resulting material.

Keywords: selective laser melting; laser powder bed fusion; metal-matrix composite; AlN; aluminum alloy; grain structure

1. Introduction

Eutectic aluminum alloy AlSi10Mg is a basic and widely used material for laser powder bed fusion (LPBF) due to its high strength and low weight [1]. Despite the high reflectivity and low laser energy absorption of aluminum alloys, it is possible to synthesize fully dense volumetric objects with complex shapes using optimal LPBF process regimes [2]. Reinforcement phase addition into aluminum creating aluminum matrix composite (AMC) is one of the ways to further improve the mechanical performance of the material. Approaches of AMCs development may be divided into "in-situ" reinforced particle formation [3] and mixing of initial matrix powder with reinforcement phases [4,5]. Significant reinforcement effect may be achieved with several aspects. First of all strength and hardness of reinforcing particles must be higher than matrix material. Moreover, particles should be uniformly distributed within the matrix to serve as barriers for dislocation movement, wherein good bonding between the matrix and reinforcements is needed. Besides the direct strengthening effect of reinforcement particles they also could lead to matrix grains refinement during so-lidification under LPBF. This effect is especially pronounced in the case of TiB_2 [6,7]. There

are many reported phases used for aluminum alloys reinforcing with different production methods such as TiC [8,9], TiN [10,11], SiC [12,13], Al_2O_3 [14,15], AlN [16,17], and other ceramics [18] providing strength, hardness, and tribological properties improvement. In the case of the LPBF process distribution of reinforcing particles within the matrix strongly depends on process parameters since laser energy input influences melting pool temperature, affecting its viscosity, and thus wetting behavior of suspended refractory particles by melt. Marangoni convection and recoil pressure [19,20] arising within the melting pool during LPBF may pull particles to the pool boundaries or instead result in their proper redistribution leading to the homogeneous distribution [14,21]. Preparation of the initial powder mixture for composite synthesis is also essential, both reinforcing particles' size and method of preparation could lead to different distribution during the LPBF process. Depending on the chemical composition and its size, the content of reinforcement particles in the AMC could vary greatly from less than a percent for nano-sized powders to tens of percent in the case of micron additives [22,23]. Common methods for the preparation of Al-based composite feedstock includes direct mixing, ball milling [24,25], direct mixing or ball milling with in situ reaction [26], in situ pre-alloying with gas atomization [27,28], agent deposition [29], electrodeposition [30].

Composites based on aluminum matrix with the addition of AlN phase are known as materials with different unique peculiarities, such as increased mechanical properties [17,31,32], wear resistance [33–35], and special thermophysical properties showing high thermal conductivity and low coefficient of thermal expansion [36–38]. The combination of high strength and hardness along with thermal stability, thermal and electrical conductivity makes aluminum nitride an indispensable component of metal matrix composites, multi-materials, and functionally graded materials for various applications in automobile, aerospace, and electronics [39–42]. Common methods of such materials synthesis are sintering, casting, infiltration, and in-situ reaction. But there are only a few studies of Al/AlN composites produced by LPBF. However, they demonstrated promising results with specific features and behavior. Dai et al. [43] provided detailed investigations of melt spreading behavior and microstructure evolution during the LPBF process using nanoscale AlN powder. Feedstock material was prepared through ball milling and optimization of synthesis parameters with a homogeneous distribution of reinforcement within the eutectic matrix. Deviation of the parameters led to nanoparticle agglomeration on the grain boundaries. Previously, authors conducted a study with submicron AlN powder [44]. Theoretical and experimental approaches also showed a strong dependence on reinforcement distribution and agglomeration on LPBF parameters and the possibility to obtain homogeneous microstructure after 3D printing. Migration and rearrangement of reinforcing particles due to thermo-capillary convection and flow were investigated. Thus, the interface of the matrix and reinforcing particles determines microstructure and mechanical properties.

Investigation of the microstructure features within the interface region is essential for various potential applications such as metal matrix composites, bimetal parts (3D printing on the substrate), functionally graded multi-materials, etc. There are several studies of grain structure and bonding features of Al/metal or Al/ceramic interfaces forming during the LPBF process. Bhaduri et al. [45] provided an investigation of AlSi10Mg built on AA6082 substrate including deep analysis of grain structure using the EBSD method. A similar study was performed by Hadadzadeh et al. [46] using an Al-Cu-Ni-Fe-Mg cast alloy substrate. Both studies dealt with alloy/alloy interfaces with similar thermophysical properties, whereas there is a lack of information concerning 3D-printed alloy/ceramic interfaces. Al/AlN interface peculiarities were analyzed in [17,47,48], but these studies were not performed under the LPBF conditions. Since the LPBF process is characterized by high-cooling rates [49], the grain structure of printed material is much finer comparing to the conventional methods. Thus, investigation of the interface region between the ceramic AlN phase and aluminum and its structure in 3d-printed materials is the key to understanding the design principles of composites and multi-materials. The current study is focused on grain structure features of the AlSi10Mg matrix in the vicinity of the AlN

reinforcing ceramic phase after the LPBF process utilizing optical microscopy, SEM, and EBSD analysis. A deep understanding of the structure formation will contribute to the development of new functionally graded composites, and multi-materials with unique mechanical, tribological, thermal and electrical properties.

2. Materials and Methods

Pure aluminum powder was used for AlN self-propagating high-temperature synthesis (SPS) in a gasostat with a 2-L volume. Tungsten-rhenium thermocouples VR5–VR20 with a diameter of 100 μm were used to determine the combustion temperature and combustion front propagation velocity. The morphology of aluminum nitride powders largely depended on the conditions of aluminum combustion in gaseous nitrogen and on the composition of the initial charge. Nitrogen pressure, the density of the initial reaction masses and their weight, and the particle size of aluminum powders were varied to obtain close to spherical morphology of AlN powder. 10 MPa nitrogen pressure, 100 g of Al powder with D50 = 62 μm, and tapped density were found as optimal conditions of the combustion process which resulted in satisfactory particle shape (see Figure 1a). A combustion temperature of 2263 K was observed. After sieving powder of 50–60 μm fraction was obtained with a distribution curve featuring two peaks (see Figure 1b).
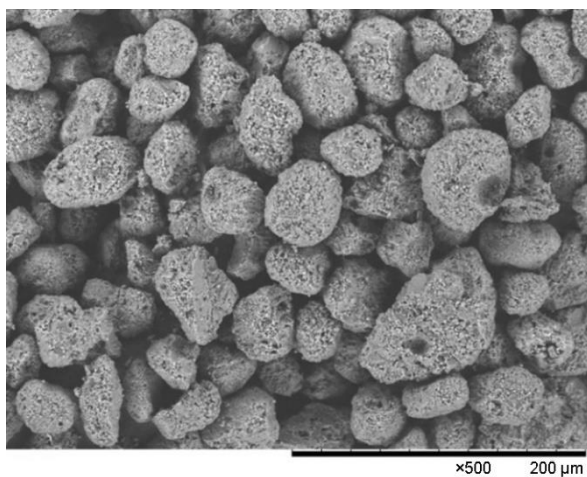
(**a**)
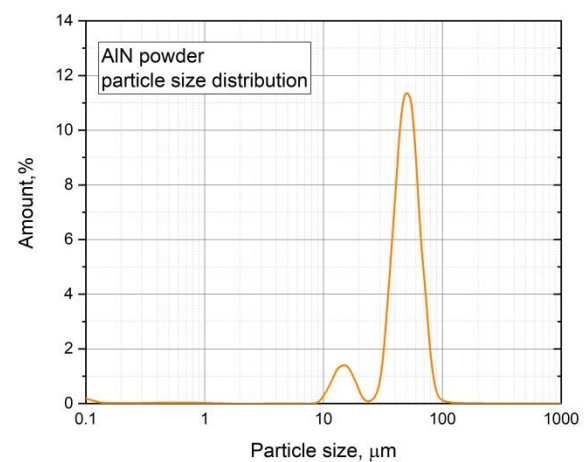
(**b**)

Figure 1. SEM image of morphology of the obtained AlN powder after sieving (**a**) and particle size distribution (**b**).

Standard gas-atomized AlSi10Mg powder (purchased from RUSAL Co., Moscow, Russia) with spherical morphology was used as a matrix material. 5 wt.% of AlN powder was added to the matrix powder and thoroughly mixed using a tumbling barrel to obtain a homogeneous distribution of reinforcing particles, which was achieved after 6 h of the process. AddSol D50 machine (Moscow, Russia) equipped with a ytterbium-fiber laser (IPG Photonics) of 400 W power with 1064 nm wavelength and 80 μm laser spot size was used for the LPBF process. Cubic samples with a 5 mm edge (see Figure 2) were printed on the aluminum substrate for further microstructure and mechanical properties investigations.

Figure 2. Cubic samples synthesized by LPBF after removing from substrate.

LPBF was carried out according to the proven method [14] to optimize the process parameters. The optimization of process parameters was performed through volumetric energy density (*ED*v, J/mm^3) of the printing process:

$$ED_V = \frac{P}{Vht};$$ (1)

where *P*—laser power, W; *V*—scan speed, mm/s; *h*—hatch distance, μm; *t*—powder layer height, μm.

A wide range of laser power and scanning speed, i.e., energy input was investigated to find the energy that ensures fully melted dense samples without defects such as pores and cracks. LPBF process parameters were selected to minimize porosity and maximize the relative density of the material, *P* and *V* were varied from 200 to 350 W and from 600 to 1400 mm/s, respectively. The layer thickness was chosen as *t* = 40 μm according to the particle size distribution of the feedstock powder. Hatch spacing *h* = 80 μm was determined as a result of single tracks analysis. The initial starting point for the process optimization was the process window for the initial AlSi10Mg powder. This material is well known for its good processability and wide processing window. Suitable process parameters for initial powder are within *ED*v = 60–120 J/mm^3 and ensure relative density higher than 99.5%. Thus, the selected initial LPBF parameters in Table 1 were within this range with varied laser power and scanning speed.

Table 1. LPBF process parameters and RD of the printed samples.

P, W	*V*, mm/s	ED_V, J/mm^3	RD, %
200	600	104.2	97.1
	800	78.1	98.4
	1000	62.5	98.2
250	800	97.7	97.6
	1000	78.1	98.9
	1200	65.1	99.3
300	1000	93.8	97.8
	1200	78.1	99.5
	1400	67.0	99.7
350	1000	109.4	97.9
	1200	91.1	99.8
	1400	78.1	99.5

The elemental composition of powder and LPBF samples were studied using X-ray fluorescent (XRF) analysis on REAN (Nauchnie pribory, St.-Petersburg, Russia) equipment

and by energy-dispersive X-ray (EDX) spectroscopy on Oxford Instruments Advanced AZtec Energy (High Wycombe, UK). X-ray diffraction (XRD) was attracted to phase composition control using a Rigaku SmartLab diffractometer (Rigaku, Tokyo, Japan). The relative material density was measured by the Archimedes method using an Adventurer Pro analytical balance (Moscow, Russia) with a measurement error of 0.001 g. The density was calculated by the following equation:

$$\rho_{sample} = \frac{m_{air}}{m_{air} - m_{liquid}}\left(\rho_{liquid} - \rho_{air}\right) + \rho_{air} \tag{2}$$

where m_{air} is the mass of the sample in the air, m_{liquid} is the mass of the sample fully submerged in isopropyl alcohol, ρ_{liquid} and ρ_{air} are liquid and air densities at measurement conditions respectively. Three measurements were made to determine the masses of the samples in air and liquid. The relative density was calculated against a theoretical density of 2.7 g·cm^{-3} for the initial mix of 95% wt. of AlSi10Mg and 5% wt. of AlN.

Particle size distribution of powders was analyzed using the laser diffraction method on the Analysette 22 NanoTecPlus device. Microstructure analysis was performed using both a Carl Zeiss A1M optical microscope (Carl Zeiss, Jena, Germany) and scanning electron microscopy (SEM) Nova NanoSEM 450 (FEI, Prague, Czech Republic). Grain structure analysis was performed using optical microscopy on polished and etched samples using Keller's reagent. The preparation of metallographic samples consisted of mechanical grinding with SiC grit papers, and final polishing using colloidal silica (3 μm and 0.25 μm). Electron backscatter diffraction (EBSD) analysis of grains crystallographic misorientation was also performed using Oxford Instruments AZtec EBSD system (High Wycombe, UK).

3. Results and Discussion

Combustion parameters were optimized to obtain the near-spherical shape of the particles, however, a developed surface was observed (see Figure 3a). Self-propagating high-temperature synthesis of aluminum nitride powder resulted in a single-phase material, which also was proven by XRD analysis (see Figure 3b). Moreover, according to EDX analysis results (see table in Figure 3) combustion process allowed to obtain of AlN composition without traces of any impurity elements.
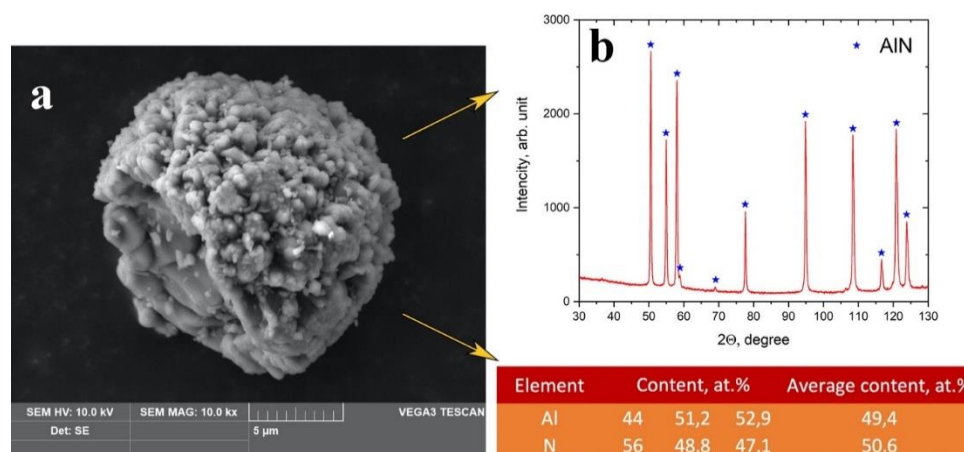

Element	Content, at.%			Average content, at.%
Al	44	51,2	52,9	49,4
N	56	48,8	47,1	50,6

Figure 3. SEM of separate AlN particle (**a**), X-ray diffraction pattern (**b**), and table with elemental composition analyzed by EDX analysis.

Since AlN particles were about 50 μm in size, XRD and EDX analysis gave information from the overall volume of particles, thus each particle had a tetrahedral crystal structure and was fully nitrided, and no core-shell structure was observed. It was also confirmed by the near 1:1 atomic concentration of the elements. The single-phase state of the material is

important for further LPBF synthesis because steady heating of the particles is provided without their partial melting, which could lead to the undesirable effect of spattering.

AlSi10Mg powder was used as matrix material with the following chemical composition: Al—87%, Si—10.7%, Mg—0.5%, Cu—0.7%, Mn—0.5%, Ti—0.2%, Fe—0.3%, other impurities—no more than 0.1%. Particle size distribution of the powder (D50 = 44 μm with SPAN = 1.38) along with high particles' sphericity meets the requirements of the LPBF process providing high flowability and apparent density. SEM images of AlSi10Mg powder morphology and particle size distribution are shown in Figure 4.
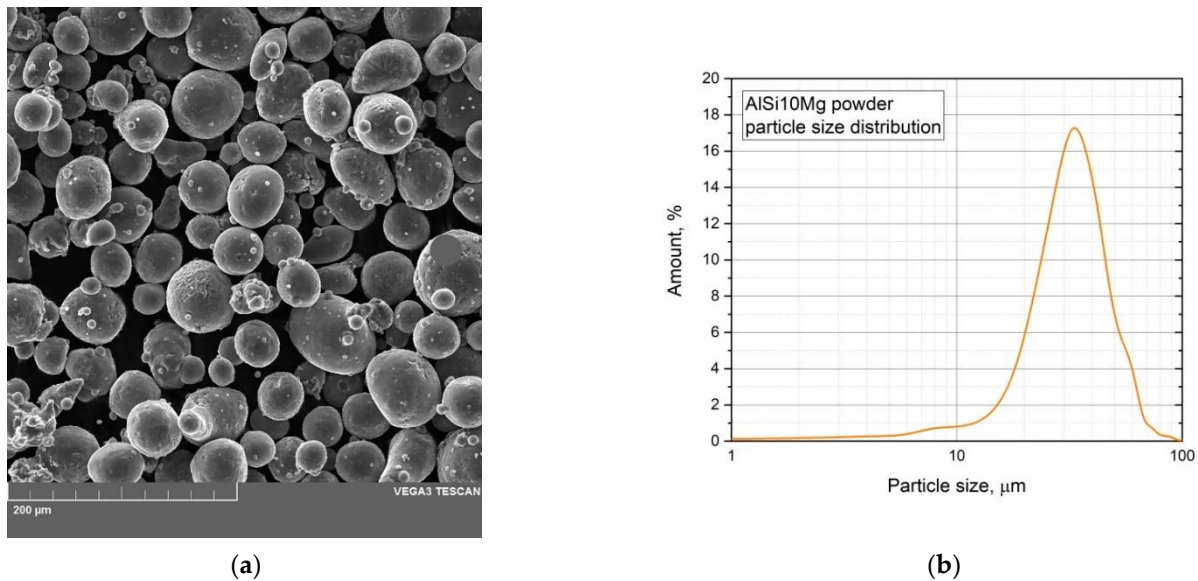

(**a**)   (**b**)

Figure 4. Morphology of AlSi10Mg matrix powder (**a**) and its particle size distribution (**b**).

Analysis of obtained samples showed relative density (RD) varied from 97.1 to 99.8%. From the results, it can be seen that the process window of powder with AlN addition moved towards lower energy densities. Moreover, higher RD was obtained in the case of process parameters with higher laser power combined with high scanning speeds. As a result, relative density numbers of more than 99.5% were obtained with 300–350 W laser power and scan speeds 1200–1400 mm/s. Such behavior is because the addition of AlN increased the overall absorptivity of the powder compared to the initial aluminum powder. This means that lower energy density is required for effective and defect-free LPBF of the powder. Therefore, the offset of the optimized process window compared to the initial AlSi10Mg alloy was achieved through the parameters with lower laser power and higher values of scan speed. Exceedance of energy density values during LPBF can lead to keyhole porosity formation and vaporization due to overheating of the powder [50,51].

Pores, unmelted areas, and cracks are typical defects inherent in the LPBF method and their ratio depends on specific material and synthesis regime. In the case of aluminum-based materials with high thermal conductivity and plasticity along with laser energy reflectivity crack formation is observed rarely, whereas different types of pores and lack of fusion defects could often arise. It is especially expected for composite materials based on aluminum matrix since reinforcing particles increase the viscosity of the melt pool [14]. Lack of fusion defects usually appears because of unsuitable LPBF process parameters and should be avoided by finding the optimal regime. Thus, the small amount of defects detected within this study is attributed to pores. Typical microstructure with pores is shown on the sample with low RD = 97.1% synthesized with P = 200 W and V = 600 mm/s (see Figure 5a (etched) and b (polished)). The sample with the highest RD = 99.8% (its microstructure is shown in Figure 5c,d) synthesized by the optimal regime (P = 350 W, V = 1200 mm/s) was chosen for further investigations.
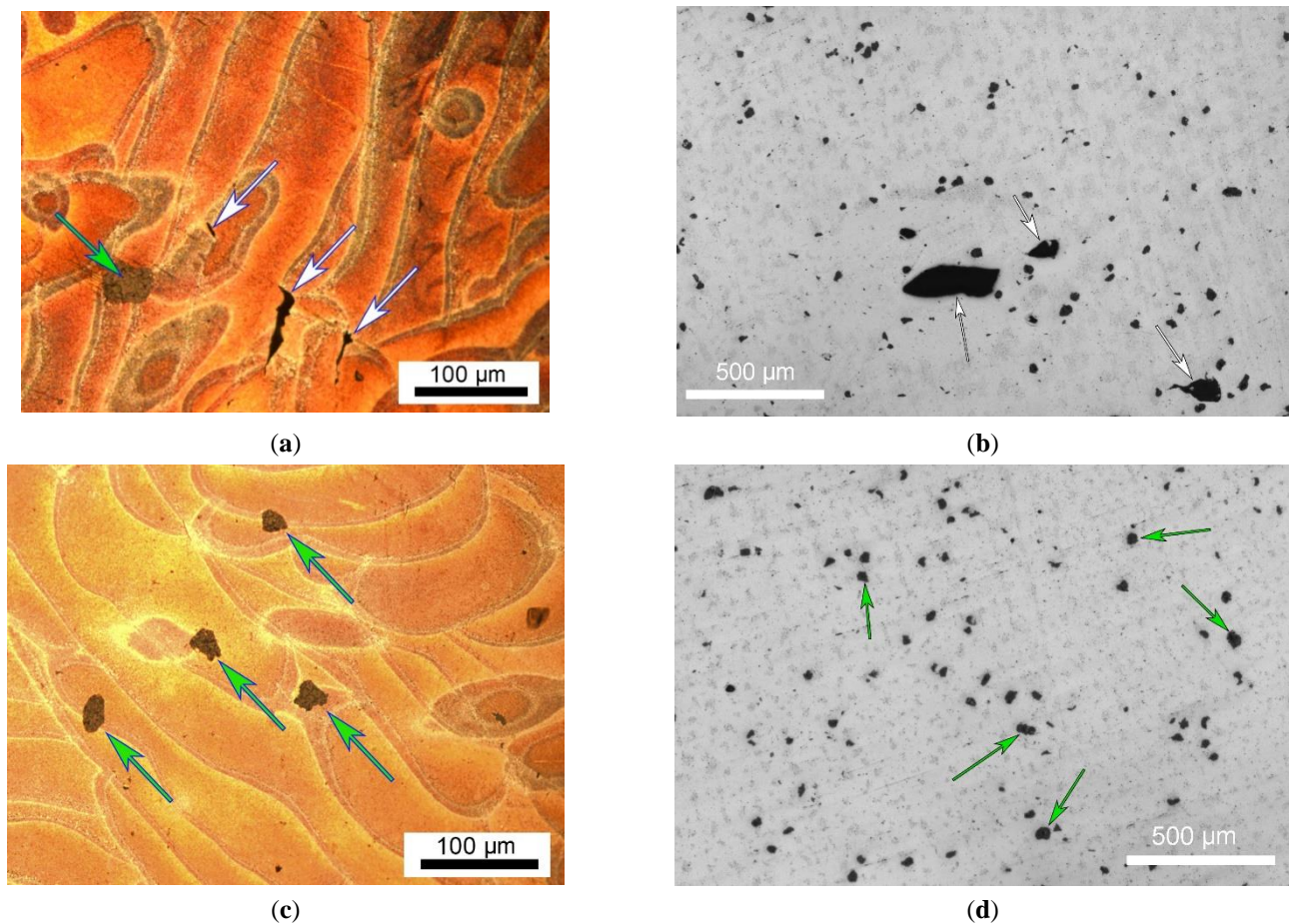
Figure 5. Optical microscopy images of etched and polished surfaces of AlSi10Mg/AlN composite printed with P = 200 W and V = 600 mm/s (**a**) and (**b**) and with P = 350 W and V = 1200 mm/s (**c**) and (**d**). Pores are shown by white arrows, whereas AlN particles are shown by green arrows.

Figure 5b,d demonstrate that AlN particles have relatively uniform distribution within the matrix despite the tendency of their pull-out to the melt pool boundaries due to the low wettability of aluminum nitride by melt. Moreover, such uniform distribution was observed regardless of porosity level. Thus, chosen process parameters window provides optimal conditions for particle rearrangement resisting their pulling from the melt by Marangoni convection.

Figure 6 shows an image of the polished and etched microstructure of AlSi10Mg/AlN composite with the highest RD = 99.8% printed by the optimal regime (P = 350 W, V = 1200 mm/s) to discern both coarse and fine-grain structures around one of the typical AlN particles. Melt pool boundaries highlighted by yellow dash lines are seen. The microstructure corresponds to the typical for AlSi10Mg in an as-built state and consists of fine grain regions (the core of the melt pool) and inhomogeneous structure around melt pool boundaries (MPB) with coarser grains [52]. Due to the directional heat sink during the LPBF process, there is a texture in the grain structure of printed materials, and in the case of XY cross-section most elongated columnar cells are seen as equiaxed. Local changes in heat sink direction led to deviation from uniaxial texture along the building direction. Such areas with deviant texture could occur near MPB, remelted or heat-affected zones, and around reinforcing particles with different thermal conductivity properties compared with the matrix. It should be noted that aluminum nitride possesses thermal conductivity is about 180 $\text{Wm}^{-1}\text{K}^{-1}$ [53] which is noticeably higher than TiB2 [54], but lower than SiC [55]. In the case of AlSi10Mg alloy high thermal conductivity of pure aluminum (247 $\text{Wm}^{-1}\text{K}^{-1}$ [56]) is decreased by alloying elements to values around 115–130 $\text{Wm}^{-1}\text{K}^{-1}$ for as-build ma-

terial [57]. Thus, the thermal conductivity of AlN particles is ~1.5 times higher than the matrix. That fact inevitably influences the crystallization process during LPBF through the change of heat dissipation conditions and hence grain structure in the vicinity of ceramic particles should differ. Superposition of build direction texture, remelting, heat-affected zones, and reinforcing particles form complex inhomogeneous grain structures with different cell orientations, sizes, and morphology. Such grain structure features could be found by analysis of Figure 6.
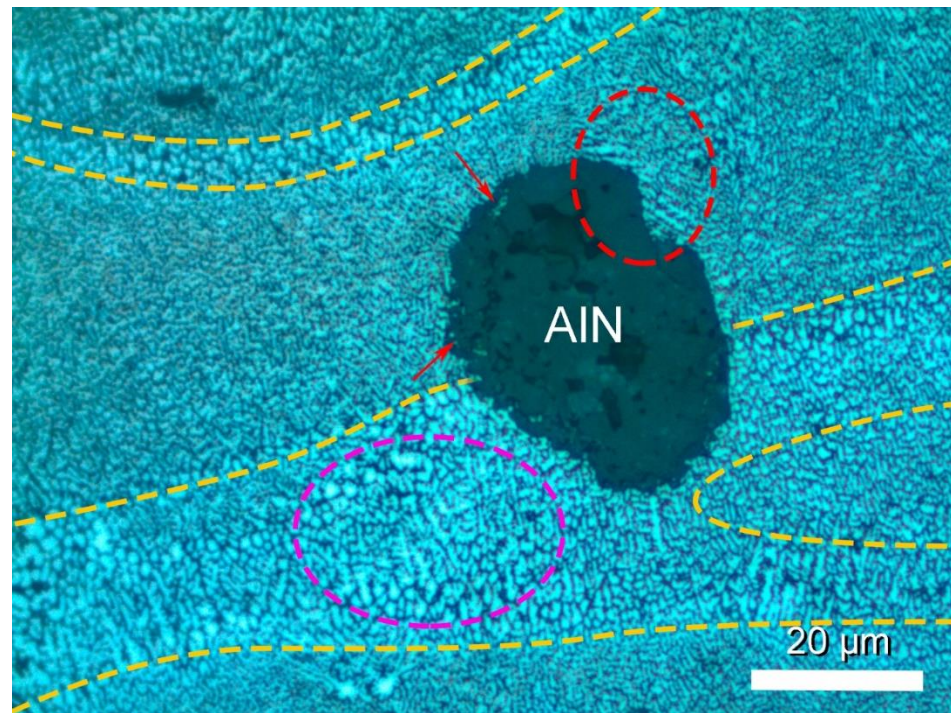

Figure 6. Optical microscopy image of the etched surface of AlSi10Mg/AlN composite after LPBF.

The region highlighted by purple circle consists mostly of coarse cells caused by remelting during the LPBF process and, thus this region was reheated after solidification which induced the recrystallization process. Such a region is usually named a heat-affected zone (HAZ). HAZs are also located along each MPB (highlighted by yellow regions) inside neighboring previous scanned track and could be seen near MPB at the «bottom» of each MP in Figure 6.

The MP in Figure 6 surrounding the AlN particle from the above has a finer structure than neighboring ones. It could be explained by the different cross-section depths of these melt pools, i.e., one MP shows the structure near the bottom of the pool whereas another demonstrates the core of the pool which experienced less heat. The most interesting features of the grain structure and texture are observed near the reinforcing particle. Some deviations from the typical structure are seen. There is a preferential centripetal orientation of grains near the interface marked by red arrows. Such features could arise due to changes in heat sink conditions because of the difference in thermal conductivity of the matrix and AlN as mentioned above. Directional crystallization is caused by the higher thermal conductivity of aluminum nitride which provided more intense heat dissipation compared to the matrix. Another feature of the grain structure marked by a red circle represents a region of coarser grains within the core of MP and near the reinforcing particle. It should be noted that the solidification mechanism in AlSi10Mg during the LPBF process is cellular-dendritic [49], and silicon is pushed into the liquid melt by the solidification front [58] saturating melt with Si. Wherein, on the one hand, the solubility of Si in Al decreases with temperature [59] but on the other hand extremely high cooling rates during LPBF,

compensate for this decrease [60]. A combination of these factors leads to solidification with cellular microstructure.

SEM analysis (see Figure 7a) was also performed on the sample with the highest RD printed by the optimal regime. EDX analysis depicted in Figure 7b confirms that light gray particles contribute to the aluminum nitride.
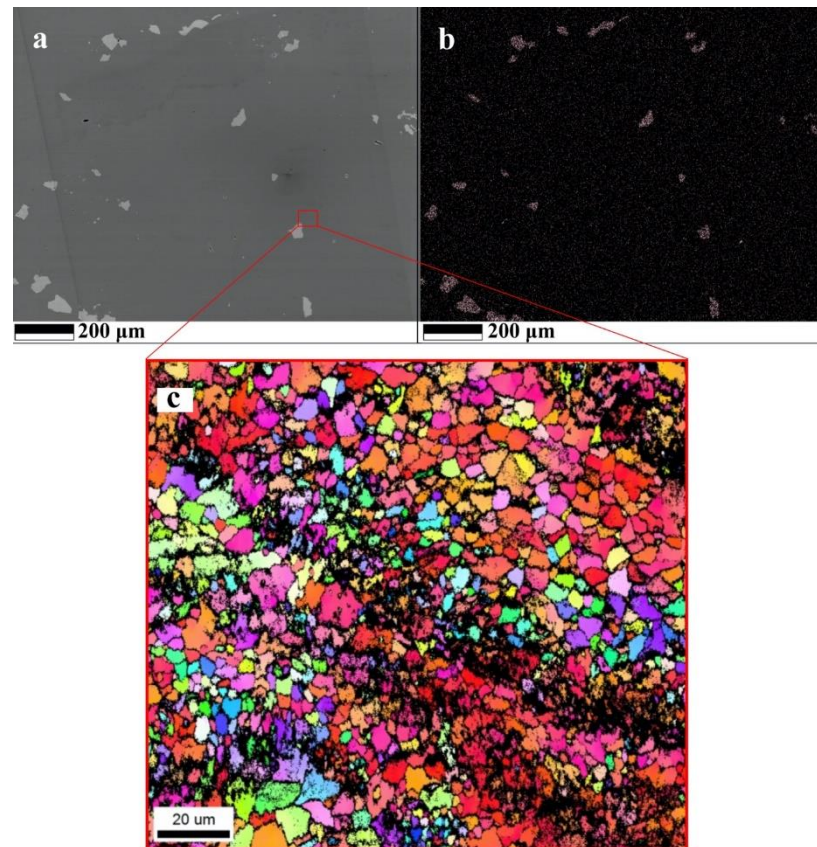

Figure 7. Images of AlSi10Mg/AlN composite polished surface (**a**), distribution of nitrogen (**b**), and EBSD map of a region near AlN particle (**c**).

EBSD analysis of grain structure also confirmed previous discussions and assumptions (see Figure 7c). The boxed-by-red area in Figure 7a was analyzed to determine grain size, texture, and crystallographic misorientation in the vicinity of the AlN particle. As it was mentioned above MPs are characterized by fine grain structure (average size 1–3 μm) whereas cores of MPBs mostly consist of relatively coarse grains with an average size of 5–7 μm. As an exception, there are a few coarse grains up to 15 μm size. The density of the black color increases in Figure 7c also indicating fine grain structure as it arises when the chosen resolution of the EBSD analysis does not allow to unambiguously determine the crystallographic orientation of a particular area. Besides fine grains distortion of lattice, high residual stress and dislocation density arising during rapid solidification also complicate the orientation calculations leading to black areas on the EBSD map. The area of coarse predominantly equiaxed grains in the lower left corresponds to the AlN particle whose structure should not be significantly changed during the LPBF process since the melting temperature of aluminum nitride is extremely high at ~2830 °C under N_2 pressure [61]. Observed and calculated temperatures of melting pool rarely exceed 2000 °C [62,63] which is far from conditions of AlN ceramic melting. Thus, the observed coarse grain structure of the ceramic was preserved after the synthesis process.

The interface between AlN and matrix has a pronounced orientation of elongated and fine matrix grains towards the ceramic particle as it was seen in Figure 6. As it was mentioned, it is explained by directional heat sink during crystallization when AlN particles

act as crystallization centers. It should be noted, that in the observed XY cross-section no texture or elongated grains are observed near the MPB but only near the interface. This fact proves the heat effect of AlN on the crystallization process and local texture formation. Wherein, according to EBSD analysis no crystallographic texture was observed neither near the interface nor in the matrix showing mostly high-angle grain boundaries. Two main factors determine grain structure near the interface region: directional heat sink and poor wettability of AlN by melt [64]. The contention of these factors leads to the formation of equiaxed fine grains besides elongated structure and texture violations.

4. Conclusions

Samples of AlSi10Mg/AlN composite were obtained through the LPBF technique using standard silumin powder mixed with aluminum nitride particles synthesized by self-propagating high-temperature synthesis. A shift of the process window to the lower values of energy density allowed to obtain samples with 99.8%. relative density after LPBF. The matrix structure has typical inhomogeneous grain size along the MP and MPB, i.e., MPBs consist of relatively coarse grains, whereas cores of MPs show finer grains. It was shown that the presence of an AlN phase with different thermo-physical characteristics influences the crystallization process of the AlSi10Mg matrix during LPBF significantly by changing the grain structure in the vicinity of the interface toward finer grains. Such fine grain structures exhibit texture directly perpendicular to the interface caused by directional heat dissipation arising due to the higher thermal conductivity of AlN. The limiting factor affecting grain refinement and directional crystallization processes is the poor wettability of AlN by melt. The combination of a directional heat sink with poor wettability determines the final microstructure of the material near the interface. Shifting the balance between the factors presumably should be regulated by the size factor, i.e., the smaller the AlN particle, the less heat sink factor contribution, and vice versa. Discovered features of the grains at the interface region between the AlN ceramic phase and AlSi10Mg matrix after the LPBF process resulted in a better understanding of the interface formation and could be helpful for further research concerning not only LPBF of composite materials but also additive manufacturing of multi-materials consisting of both metals and ceramics.

Author Contributions: Conceptualization, A.Y.N. and A.A.G.; methodology, D.Y.O. and A.I.B.; investigation, S.V.C., B.O.Z. and A.I.B.; writing—original draft preparation, I.A.P.; writing—review and editing, D.Y.O. and A.A.G.; visualization, A.V.K.; supervision, A.A.G. All authors have read and agreed to the published version of the manuscript.

Institutional Review Board Statement: Not applicable.

Informed Consent Statement: Not applicable.

Data Availability Statement: The data presented in this study are available on request from the corresponding author. The data are not publicly available due to privacy.

Conflicts of Interest: The authors declare no conflict of interest.

References

1. Brandl, E.; Heckenberger, U.; Holzinger, V.; Buchbinder, D. Additive manufactured AlSi10Mg samples using Selective Laser Melting (SLM): Microstructure, high cycle fatigue, and fracture behavior. *Mater. Des.* **2012**, *34*, 159–169. [CrossRef]
2. Maamoun, A.; Xue, Y.; Elbestawi, M.; Veldhuis, S. Effect of Selective Laser Melting Process Parameters on the Quality of Al Alloy Parts: Powder Characterization, Density, Surface Roughness, and Dimensional Accuracy. *Materials* **2018**, *11*, 2343. [CrossRef] [PubMed]
3. Dadbakhsh, S.; Mertens, R.; Hao, L.; Van Humbeeck, J.; Kruth, J.P. Selective Laser Melting to Manufacture "In Situ" Metal Matrix Composites: A Review. *Adv. Eng. Mater.* **2019**, *21*, 1801244. [CrossRef]

4. Yuan, P.; Gu, D.; Dai, D. Particulate migration behavior and its mechanism during selective laser melting of TiC reinforced Al matrix nanocomposites. *Mater. Des.* **2015**, *82*, 46–55. [CrossRef]

5. Zhao, X.; Song, B.; Fan, W.; Zhang, Y.; Shi, Y. Selective laser melting of carbon/AlSi10Mg composites: Microstructure, mechanical and electronical properties. *J. Alloys Compd.* **2016**, *665*, 271–281. [CrossRef]

6. Karbalaei Akbari, M.; Baharvandi, H.R.; Shirvanimoghaddam, K. Tensile and fracture behavior of nano/micro TiB2 particle reinforced casting A356 aluminum alloy composites. *Mater. Des.* **2015**, *66*, 150–161. [CrossRef]

7. Xi, L.X.; Zhang, H.; Wang, P.; Li, H.C.; Prashanth, K.G.; Lin, K.J.; Kaban, I.; Gu, D.D. Comparative investigation of microstructure, mechanical properties and strengthening mechanisms of Al-12Si/TiB2 fabricated by selective laser melting and hot pressing. *Ceram. Int.* **2018**, *44*, 17635–17642. [CrossRef]

8. Gopalakrishnan, S.; Murugan, N. Production and wear characterisation of AA 6061 matrix titanium carbide particulate reinforced composite by enhanced stir casting method. *Compos. Part B Eng.* **2012**, *43*, 302–308. [CrossRef]

9. Gu, D.; Wang, H.; Dai, D.; Yuan, P.; Meiners, W.; Poprawe, R. Rapid fabrication of Al-based bulk-form nanocomposites with novel reinforcement and enhanced performance by selective laser melting. *Scr. Mater.* **2015**, *96*, 25–28. [CrossRef]

10. Gao, C.; Wu, W.; Shi, J.; Xiao, Z.; Akbarzadeh, A.H. Simultaneous enhancement of strength, ductility, and hardness of TiN/AlSi10Mg nanocomposites via selective laser melting. *Addit. Manuf.* **2020**, *34*, 101378. [CrossRef]

11. Gao, C.; Xiao, Z.; Liu, Z.; Zhu, Q.; Zhang, W. Selective laser melting of nano-TiN modified AlSi10Mg composite powder with low laser reflectivity. *Mater. Lett.* **2019**, *236*, 362–365. [CrossRef]

12. Chang, F.; Gu, D.; Dai, D.; Yuan, P. Selective laser melting of in-situ Al4SiC4 + SiC hybrid reinforced Al matrix composites: Influence of starting SiC particle size. *Surf. Coatings Technol.* **2015**, *272*, 15–24. [CrossRef]

13. Xue, G.; Ke, L.; Zhu, H.; Liao, H.; Zhu, J.; Zeng, X. Influence of processing parameters on selective laser melted SiCp/AlSi10Mg composites: Densification, microstructure and mechanical properties. *Mater. Sci. Eng. A* **2019**, *764*, 138155. [CrossRef]

14. Pelevin, I.A.; Nalivaiko, A.Y.; Ozherelkov, D.Y.; Shinkaryov, A.S.; Chernyshikhin, S.V.; Arnautov, A.N.; Zmanovsky, S.V.; Gromov, A.A. Selective Laser Melting of Al-Based Matrix Composites with Al2O3 Reinforcement: Features and Advantages. *Materials* **2021**, *14*, 2648. [CrossRef] [PubMed]

15. Han, Q.; Setchi, R.; Lacan, F.; Gu, D.; Evans, S.L. Selective laser melting of advanced Al-Al 2 O 3 nanocomposites: Simulation, microstructure and mechanical properties. *Mater. Sci. Eng. A* **2017**, *698*, 162–173. [CrossRef]

16. Cho, S.C.; Han, C.; Choi, H.; Kim, H.S.; Jin, S.; Han, J.H. Synthesis and consolidation behavior of Al/AlN composite powders by reactive RF thermal plasma spraying. *Powder Technol.* **2016**, *287*, 395–402. [CrossRef]

17. Liu, Y.Q.; Cong, H.T.; Wang, W.; Sun, C.H.; Cheng, H.M. AlN nanoparticle-reinforced nanocrystalline Al matrix composites: Fabrication and mechanical properties. *Mater. Sci. Eng. A* **2009**, *505*, 151–156. [CrossRef]

18. Pramod, S.L.; Bakshi, S.R.; Murty, B.S. Aluminum-Based Cast In Situ Composites: A Review. *J. Mater. Eng. Perform.* **2015**, *24*, 2185–2207. [CrossRef]

19. Liu, Y.; Yang, Y.; Mai, S.; Wang, D.; Song, C. Investigation into spatter behavior during selective laser melting of AISI 316L stainless steel powder. *Mater. Des.* **2015**, *87*, 797–806. [CrossRef]

20. Olakanmi, E.O.; Cochrane, R.F.; Dalgarno, K.W. A review on selective laser sintering/melting (SLS/SLM) of aluminium alloy powders: Processing, microstructure, and properties. *Prog. Mater. Sci.* **2015**, *74*, 401–477. [CrossRef]

21. Yuan, P.; Gu, D. Molten pool behaviour and its physical mechanism during selective laser melting of TiC/AlSi10Mg nanocomposites: Simulation and experiments. *J. Phys. D. Appl. Phys.* **2015**, *48*, 035303. [CrossRef]

22. Gu, D.; Yuan, P. Thermal evolution behavior and fluid dynamics during laser additive manufacturing of Al-based nanocomposites: Underlying role of reinforcement weight fraction. *J. Appl. Phys.* **2015**, *118*, 233109. [CrossRef]

23. Gu, D.; Rao, X.; Dai, D.; Ma, C.; Xi, L.; Lin, K. Laser additive manufacturing of carbon nanotubes (CNTs) reinforced aluminum matrix nanocomposites: Processing optimization, microstructure evolution and mechanical properties. *Addit. Manuf.* **2019**, *29*, 100801. [CrossRef]

24. Gu, D.; Ma, C.; Xia, M.; Dai, D.; Shi, Q. A Multiscale Understanding of the Thermodynamic and Kinetic Mechanisms of Laser Additive Manufacturing. *Engineering* **2017**, *3*, 675–684. [CrossRef]

25. Han, Q.; Setchi, R.; Evans, S.L. Synthesis and characterisation of advanced ball-milled Al-Al2O3 nanocomposites for selective laser melting. *Powder Technol.* **2016**, *297*, 183–192. [CrossRef]

26. Dadbakhsh, S.; Hao, L. Effect of Al alloys on selective laser melting behaviour and microstructure of in situ formed particle reinforced composites. *J. Alloys Compd.* **2012**, *541*, 328–334. [CrossRef]

27. Li, X.P.; Ji, G.; Chen, Z.; Addad, A.; Wu, Y.; Wang, H.W.; Vleugels, J.; Van Humbeeck, J.; Kruth, J.P. Selective laser melting of nano-TiB 2 decorated AlSi10Mg alloy with high fracture strength and ductility. *Acta Mater.* **2017**, *129*, 183–193. [CrossRef]

28. Chen, M.; Li, X.; Ji, G.; Wu, Y.; Chen, Z.; Baekelant, W.; Vanmeensel, K.; Wang, H.; Kruth, J.-P. Novel Composite Powders with Uniform TiB2 Nano-Particle Distribution for 3D Printing. *Appl. Sci.* **2017**, *7*, 250. [CrossRef]

29. Tan, H.; Hao, D.; Al-Hamdani, K.; Zhang, F.; Xu, Z.; Clare, A.T. Direct metal deposition of TiB 2 /AlSi10Mg composites using satellited powders. *Mater. Lett.* **2018**, *214*, 123–126. [CrossRef]

30. Martin, J.H.; Yahata, B.D.; Hundley, J.M.; Mayer, J.A.; Schaedler, T.A.; Pollock, T.M. 3D printing of high-strength aluminium alloys. *Nature* **2017**, *549*, 365–369. [CrossRef]

31. Troadec, C.; Goeuriot, P.; Verdier, P.; Laurent, Y.; Vicens, J.; Boitier, G.; Chermant, J.L.; Mordike, B.L. AlN dispersed reinforced aluminum composite. *J. Eur. Ceram. Soc.* **1997**, *17*, 1867–1875. [CrossRef]

32. Yu, P.; Balog, M.; Yan, M.; Schaffer, G.B.; Qian, M. In situ fabrication and mechanical properties of Al–AlN composite by hot extrusion of partially nitrided AA6061 powder. *J. Mater. Res.* **2011**, *26*, 1719–1725. [CrossRef]

33. Wahab, M.N.; Ghazali, M.J.; Daud, A.R. Effect of Aluminum Nitride (AlN) Addition on Wear and Mechanical Properties of Al-Si Alloy Composites Fabricated by Stir Casting Process. *Key Eng. Mater.* **2011**, *462–463*, 307–312. [CrossRef]

34. Fale, S.; Likhite, A.; Bhatt, J. The Wear Behavior of In-Situ Al–AlN Metal Matrix Composites. *Trans. Indian Inst. Met.* **2014**, *67*, 841–849. [CrossRef]

35. Mathan Kumar, N.; Senthil Kumaran, S.; Kumaraswamidhas, L.A. Wear behaviour of Al 2618 alloy reinforced with Si 3 N 4, AlN and ZrB 2 in situ composites at elevated temperatures. *Alexandria Eng. J.* **2016**, *55*, 19–36. [CrossRef]

36. Balog, M.; Yu, P.; Qian, M.; Behulova, M.; Svec, P.; Cicka, R. Nanoscaled Al–AlN composites consolidated by equal channel angular pressing (ECAP) of partially in situ nitrided Al powder. *Mater. Sci. Eng. A* **2013**, *562*, 190–195. [CrossRef]

37. Mizuuchi, K.; Inoue, K.; Agari, Y.; Nagaoka, T.; Sugioka, M.; Tanaka, M.; Takeuchi, T.; Tani, J.; Kawahara, M.; Makino, Y.; et al. Processing and thermal properties of Al/AlN composites in continuous solid–liquid co-existent state by spark plasma sintering. *Compos. Part B Eng.* **2012**, *43*, 1557–1563. [CrossRef]

38. Couturier, R.; Ducret, D.; Merle, P.; Disson, J.P.; Joubert, P. Elaboration and characterization of a metal matrix composite: Al/AlN. *J. Eur. Ceram. Soc.* **1997**, *17*, 1861–1866. [CrossRef]

39. Xiu, Z.; Ju, B.; Liu, S.; Song, Y.; Du, J.; Li, Z.; Zhou, C.; Yang, W.; Wu, G. Spark Plasma Sintering of AlN/Al Functionally Graded Materials. *Materials* **2021**, *14*, 4893. [CrossRef]

40. Dun, B.; Jia, X.; Jia, C.; Chu, K. Thermal conductivity behavior of SPS consolidated AlN/Al composites for thermal management applications. *Rare Met.* **2011**, *30*, 189–194. [CrossRef]

41. Amosov, A.P.; Titova, Y.V.; Timoshkin, I.Y.; Kuzina, A.A. Fabrication of Al-AlN Nanocomposites. *Key Eng. Mater.* **2016**, *684*, 302–309. [CrossRef]

42. Kondoh, K.; Takeda, Y.; Kimura, A. Wear Properties of In-Situ Reacted Al-AlN Composite Sintered Material and Application for Automatic Transmission Parts. In Proceedings of the SAE Technical Papers, Detroit, MI, USA, 1-4 March 1999.

43. Dai, D.; Gu, D.; Xia, M.; Ma, C.; Chen, H.; Zhao, T.; Hong, C.; Gasser, A.; Poprawe, R. Melt spreading behavior, microstructure evolution and wear resistance of selective laser melting additive manufactured AlN/AlSi10Mg nanocomposite. *Surf. Coatings Technol.* **2018**, *349*, 279–288. [CrossRef]

44. Dai, D.; Gu, D. Influence of thermodynamics within molten pool on migration and distribution state of reinforcement during selective laser melting of AlN/AlSi10Mg composites. *Int. J. Mach. Tools Manuf.* **2016**, *100*, 14–24. [CrossRef]

45. Bhaduri, D.; Penchev, P.; Essa, K.; Dimov, S.; Carter, L.N.; Pruncu, C.I.; Pullini, D. Evaluation of surface/interface quality, microstructure and mechanical properties of hybrid additive-subtractive aluminium parts. *CIRP Ann.* **2019**, *68*, 237–240. [CrossRef]

46. Hadadzadeh, A.; Amirkhiz, B.S.; Shakerin, S.; Kelly, J.; Li, J.; Mohammadi, M. Microstructural investigation and mechanical behavior of a two-material component fabricated through selective laser melting of AlSi10Mg on an Al-Cu-Ni-Fe-Mg cast alloy substrate. *Addit. Manuf.* **2020**, *31*, 100937. [CrossRef]

47. Nagatomo, Y.; Kitahara, T.; Nagase, T.; Kuromitsu, Y.; Sosiati, H.; Kuwano, N. Changes in Microstructure of Al/AlN Interface during Thermal Cycling. *Mater. Trans.* **2008**, *49*, 2808–2814. [CrossRef]

48. Chen, C.; Cui, C.; Zhao, L.; Liu, S.; Liu, S. The formation mechanism and interface structure characterization of in situ AlN/Al composites. *J. Compos. Mater.* **2016**, *50*, 495–506. [CrossRef]

49. Aboulkhair, N.T.; Simonelli, M.; Parry, L.; Ashcroft, I.; Tuck, C.; Hague, R. 3D printing of Aluminium alloys: Additive Manufacturing of Aluminium alloys using selective laser melting. *Prog. Mater. Sci.* **2019**, *106*, 100578. [CrossRef]

50. Oliveira, J.P.; LaLonde, A.D.; Ma, J. Processing parameters in laser powder bed fusion metal additive manufacturing. *Mater. Des.* **2020**, *193*, 108762. [CrossRef]

51. Gu, D.; Wang, H.; Chang, F.; Dai, D.; Yuan, P.; Hagedorn, Y.-C.; Meiners, W. Selective Laser Melting Additive Manufacturing of TiC/AlSi10Mg Bulk-form Nanocomposites with Tailored Microstructures and Properties. *Phys. Procedia* **2014**, *56*, 108–116. [CrossRef]

52. Xiong, Z.H.; Liu, S.L.; Li, S.F.; Shi, Y.; Yang, Y.F.; Misra, R.D.K. Role of melt pool boundary condition in determining the mechanical properties of selective laser melting AlSi10Mg alloy. *Mater. Sci. Eng. A* **2019**, *740–741*, 148–156. [CrossRef]

53. Wallis, C.; Buchmayr, B.; Bermejo, R.; Supancic, P. Fabrication of 3D metal-ceramic (Al-AlN) architectures using laser-powder bed fusion process. *Addit. Manuf.* **2021**, *38*, 101799. [CrossRef]

54. Munro, R.G. Material properties of titanium diboride. *J. Res. Natl. Inst. Stand. Technol.* **2000**, *105*, 709. [CrossRef]

55. Zheng, Q.; Li, C.; Rai, A.; Leach, J.H.; Broido, D.A.; Cahill, D.G. Thermal conductivity of GaN, GaN71, and SiC from 150 K to 850 K. *Phys. Rev. Mater.* **2019**, *3*, 014601. [CrossRef]

56. Chung, D.D. Materials for thermal conduction. *Appl. Therm. Eng.* **2001**, *21*, 1593–1605. [CrossRef]

57. Sélo, R.R.J.; Catchpole-Smith, S.; Maskery, I.; Ashcroft, I.; Tuck, C. On the thermal conductivity of AlSi10Mg and lattice structures made by laser powder bed fusion. *Addit. Manuf.* **2020**, *34*, 101214. [CrossRef]

58. Prashanth, K.G.; Scudino, S.; Klauss, H.J.; Surreddi, K.B.; Löber, L.; Wang, Z.; Chaubey, A.K.; Kühn, U.; Eckert, J. Microstructure and mechanical properties of Al–12Si produced by selective laser melting: Effect of heat treatment. *Mater. Sci. Eng. A* **2014**, *590*, 153–160. [CrossRef]

59. Bose, S.K.; Kumar, R. Structure of rapidly solidified aluminium-silicon alloys. *J. Mater. Sci.* **1973**, *8*, 1795–1799. [CrossRef]

60. Birol, Y. Microstructural evolution during annealing of a rapidly solidified Al–12Si alloy. *J. Alloys Compd.* **2007**, *439*, 81–86. [CrossRef]
61. Gillan, E.G. Precursor Chemistry—Group 13 Nitrides and Phosphides (Al, Ga, and In). In *Comprehensive Inorganic Chemistry II*; Elsevier: Amsterdam, The Netherlands, 2013; Volume 1, pp. 969–1000.
62. Sun, S.; Zheng, L.; Liu, Y.; Liu, J.; Zhang, H. Selective laser melting of Al-Fe-V-Si heat-resistant aluminum alloy powder: Modeling and experiments. *Int. J. Adv. Manuf. Technol.* **2015**, *80*, 1787–1797. [CrossRef]
63. Liu, S.; Zhu, J.; Zhu, H.; Yin, J.; Chen, C.; Zeng, X. Effect of the track length and track number on the evolution of the molten pool characteristics of SLMed Al alloy: Numerical and experimental study. *Opt. Laser Technol.* **2020**, *123*, 105924. [CrossRef]
64. Nicholas, M.G.; Mortimer, D.A.; Jones, L.M.; Crispin, R.M. Some observations on the wetting and bonding of nitride ceramics. *J. Mater. Sci.* **1990**, *25*, 2679–2689. [CrossRef]